

# On the Origin of Supertetragonality in BaTiO<sub>3</sub>

S. Mellaerts<sup>1</sup>, J.W. Seo<sup>2</sup>, V. Afanas'ev<sup>1</sup>, M. Houssa<sup>1,3</sup> and J.-P. Locquet<sup>1</sup>

<sup>1</sup>*Department of Physics and Astronomy, KU Leuven, Celestijnenlaan 200D, 3001 Leuven, Belgium,* <sup>2</sup>*Department of Materials Engineering, KU Leuven, Kasteelpark Arenberg 44, 3001 Leuven, Belgium,* <sup>3</sup>*Imec, Kapeldreef 75, 3001 Leuven, Belgium\**

Understanding ferroelectricity is of both fundamental and technological importance to further stimulate the development of new materials designs and manipulations. Here, we perform an in-depth first-principle study on the well-known ferroelectric barium titanate BaTiO<sub>3</sub> under a hydrostatic negative pressure, showing an isosymmetric phase transition to a supertetragonal phase with high  $c/a$  ratio of  $\sim 1.3$ . The microscopic origin and driving mechanisms of this phase transition are identified as a drastic change of the covalently  $\pi$ -bonded electrons. These findings provide guidance in the search for new supertetragonal phases, with great opportunities for novel multiferroic materials; and can be generalized in the understanding of other isosymmetric phase transitions.

## I. INTRODUCTION

Complex metal oxides host a rich variety of functional properties - including multiferroicity, dielectricity, metal-insulator transitions and topological phases - that can be controlled by doping and epitaxial strain [1, 2]. This tunability has strongly motivated the technological interest in these metal oxides, and although past decades have witnessed great efforts in fundamental research, there remains a great need for novel materials designs and manipulations. The former has been an essential pathway to find new multiferroic systems, and to the exploration of double perovskites [3, 4] as well as the idea of ferroelectric materials driven by polar octahedral rotations [5, 6], while for the latter the development of vertically aligned nanocomposites (VANs) has recently attracted great attention [7–12]. For example, an enhanced Curie temperature of 616°C in BaTiO<sub>3</sub> has been induced through negative pressure [11].

This experimental effort towards three-dimensional (3D) strain opens a largely unexplored region in phase space, experimentally as well as computationally. Ultimately, it might open the path in fulfilling the dream of having a complete atomic control of the transition metal within the oxygen octahedron and its corresponding distortions.

In this work, we study BaTiO<sub>3</sub> as a model system and perform a first-principle study under hydrostatic negative pressure. BaTiO<sub>3</sub> is particularly interesting owing to its excellent lead-free ferroelectricity as well as piezoelectricity. Its possibility to grow epitaxially on silicon substrates using SrTiO<sub>3</sub> buffer layers [13–15] enables the integration into silicon platforms which has gained significant interest [16–18]. Our results demonstrate a first-order transition to a supertetragonal (ST) phase with  $c/a \sim 1.3$ , which has also been observed in PbTiO<sub>3</sub> nanowires upon negative pressure [19, 20], as well as

in highly strained BiFeO<sub>3</sub> [21, 22]. However, a firm understanding of the chemical origin of this ST phase has remained absent. By a detailed first-principle based analysis on the intimate mixed ionic-covalent nature of BaTiO<sub>3</sub>, we identify the key changes in the electronic structure that drive the supertetragonal phase transition.

## II. BaTiO<sub>3</sub> PHASES

As a first part of this study, all four BaTiO<sub>3</sub> phases - cubic ( $Pm\bar{3}m$ ), tetragonal ( $P4mm$ ), orthorhombic ( $Amm2$ ) and rhombohedral ( $R3m$ ) - are being studied on a structural and dielectric level. All calculations were performed by the use of the PBEsol functional as it has shown to be one of the most accurate exchange-correlations functionals for the various ferroelectric perovskites [23, 24]. The resulting properties of the high-temperature ( $Pm\bar{3}m$  and  $P4mm$ ) and low-temperature phases ( $Amm2$  and  $R3m$ ) have been summarized in Table I and II, respectively.

Table I. A structural and dielectric comparison of the cubic ( $Pm\bar{3}m$ ) and tetragonal ( $P4mm$ ) BaTiO<sub>3</sub> phases, with a comparison to their experimental values. The optical dielectric function  $\epsilon^\infty$ , Born effective charges of titanium  $Z_{Ti}^*$  and total polarization  $P_s$  are given.

	Cubic ( $Pm\bar{3}m$ )	
	Theory	Experiment
$a$ (Å)	3.985	3.996 [25]
$\epsilon_{ii}^\infty$	6.79	5.40 [26]
$(Z_{Ti}^*)_{ii}$	7.41	/
	Tetragonal ( $P4mm$ )	
	Theory	Experiment
$a$ (Å)	3.968	3.995 [27]
$c$ (Å)	4.072	4.034 [27]
$(\epsilon_{11}^\infty, \epsilon_{33}^\infty)$	(6.45, 5.66)	(5.93, 5.60) [28]
$(Z_{Ti}^*)_{ii}$	(7.05, 7.05, 5.61)	/
$P_s$ ( $\mu\text{C}/\text{cm}^2$ )	35.7	26.0 [29]

\* simon.mellaerts@kuleuven.be

For the structural parameters, an excellent agreement with the experimental results could be achieved, while for the dielectric properties, there exists a small overestimation attributed to the usual delocalized tendency of the DFT exchange-correlation functionals.

Table II. A structural and dielectric comparison of the low-temperature orthorhombic ( $Amm2$ ) and rhombohedral ( $R3m$ )  $BaTiO_3$  phases, with a comparison to their experimental values.

	Orthorhombic ( $Amm2$ )	
	Theory	Experiment
$a$ (Å)	3.961	3.983 [30]
$b$ (Å)	5.686	5.674 [30]
$c$ (Å)	5.709	5.692 [30]
$\epsilon_{ii}^\infty$	(6.35, 6.06, 5.63)	/
$(Z_{Ti}^*)_{ii}$	(6.94, 6.42, 5.58)	/
$P_s$ ( $\mu C/cm^2$ )	44.8	/
	Rhombohedral ( $R3m$ )	
	Theory	Experiment
$a$ (Å)	4.007	4.004 [30]
$\alpha$ ( $^\circ$ )	89.85	89.84 [30]
$\epsilon_{ii}^\infty$	(5.95, 5.95, 5.95)	/
$\epsilon_{ij}^\infty$ ( $i \neq j$ )	-0.16	/
$(Z_{Ti}^*)_{ii}$	(6.22, 6.22, 6.22)	/
$(Z_{Ti}^*)_{ij}$ ( $i \neq j$ )	-0.32	/
$P_s$ ( $\mu C/cm^2$ )	47.9	34 [31]

The rich phase diagram of  $BaTiO_3$  is in stark contrast to  $PbTiO_3$  that has only the tetragonal phase as ground state. This is often ascribed to the lone pair of  $6s$  electrons of  $Pb^{2+}$  overlapping with the oxygen orbitals to attain a lobe shape [32], breaking the spherical symmetry and imposing restrictions on the Ti off-centring to one single direction. While for  $BaTiO_3$ , electronegativity analysis shows a 82% ionic component in the Ba–O bond [33], which allows to consider it fully ionic within a first approximation. Therefore,  $Ba^{2+}$  imposes no symmetry restriction on the Ti off-centring, giving rise to its rich phase diagram, where the sequence of phase transitions as a function of temperature can be conceived as a tendency to maximize the covalent bonding of the titanium with the oxygens corners of the octahedron.

In the cubic structure, the  $Ti^{4+}$  in the oxygen octahedra has  $O_h$  symmetry where the crystal field splits the five-fold degenerate  $d$ -orbital into a triple degenerate  $t_{2g}$  ( $d_{xy}, d_{xz}, d_{yz}$ ) lower level and the double degenerate  $e_g$  ( $d_{x^2-y^2}, d_{z^2}$ ) level (see Figure 1). This latter  $e_g$  orbital level forms a  $\sigma$ -bond with all six oxygen  $p$ -orbitals. More specifically, within valence band theory, these hybridize with the Ti  $4s$  and  $4p$  orbital to form  $sp^3d^2$  hybrid orbital with six lobes oriented towards the linear  $sp$  oxygen hybrid orbitals, giving rise to six equivalent  $\sigma$ -bonds. In addition,  $\pi$  molecular orbitals are formed perpendicular

to the O–Ti–O direction by the  $t_{2g}$  states, which are degenerate and mutually orthogonal. Because of the 37% covalent component in the Ti–O bond [33], the triple degenerate ( $d_{xy}, d_{xz}, d_{yz}$ ) orbitals and their bonding dominate the ferroelectric distortion, as they allow to weaken and overcome the spherical symmetric short-range ionic repulsion [34]. In the cubic structure, these orbitals form a nearly spherical symmetric delocalized electron cloud within the octahedron, with weak negligible covalent bonds. Upon tetragonal distortion (see Fig. 2b), the  $\pi$ -bond along the polar  $z$ -axis will be strengthened with an increasing orbital overlap of the ( $d_{xz}, d_{yz}$ ) orbitals with the  $O_3$  ( $p_x, p_y$ ) orbitals. Further lowering the temperature, forces the Ti off-centring to the (110) direction with a further covalent enhancement of the  $\pi$ -bond with two oxygens in the orthorhombic phase, and finally a Ti off-centring to the (111) direction in the rhombohedral phase with three strong  $\pi$ -bonds formed [35–37].

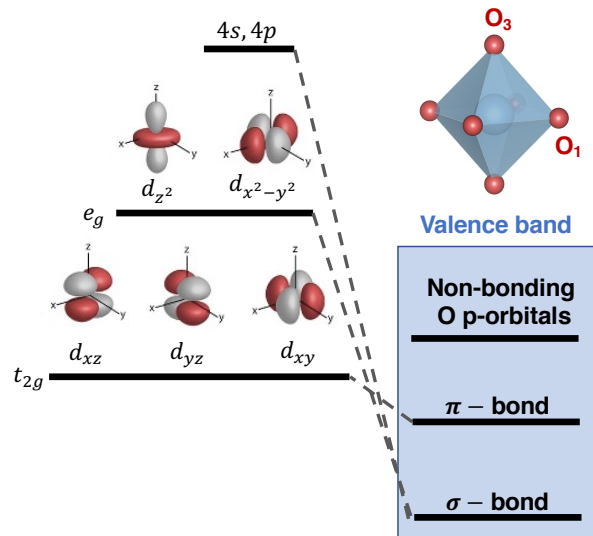


Figure 1. The chemical bonding in  $BaTiO_3$ . The octahedral crystal field splits the  $3d$  orbitals into  $t_{2g}$  and  $e_g$  which are involved in the  $\sigma$ - and  $\pi$ -bond, such that the valence band mainly consists of the covalent bonded Ti  $3d$ -orbitals and O  $2p$ -orbitals.

Understanding the sequence of phase transitions within this molecular orbital description is also informative in understanding the dielectric trend for the different  $BaTiO_3$  phases. The increasing covalent bonding tendency results in reduced dielectric constant and Born charges upon transitioning to the low-T phases, as the charge is no longer delocalized within the octahedron but rather forms well-defined bonding orbitals. In other words, the transition to the lower symmetry phase implies an enhanced covalency with well-defined directionality - because a purely ionic compound will have the highest structural symmetry - and with the counter-intuitive localization of the electrons within the octahedron as the symmetry is lowered.

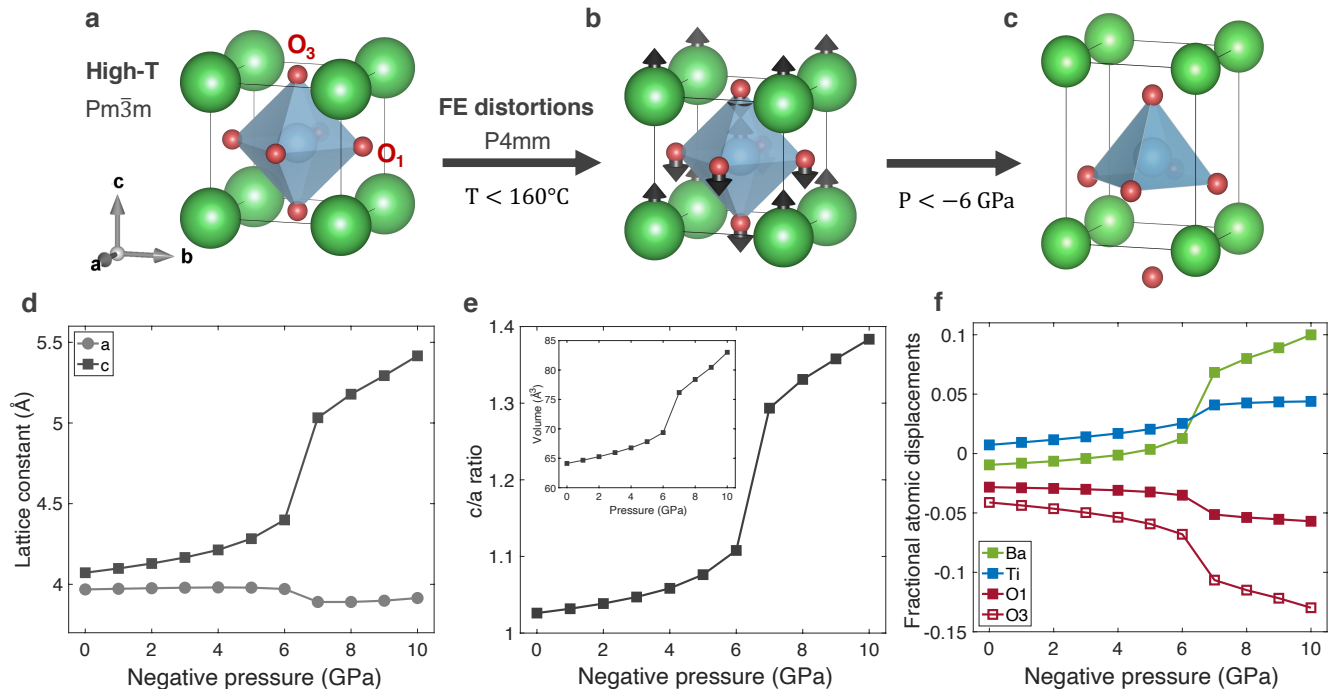


Figure 2. The structural component of the supertetragonal phase transition. The crystal structures of (a) the high-temperature cubic crystal structure, (b) the corresponding ferroelectric (FE) polar distortion, and (c) the supertetragonal phase found in the negative pressure regime. (d) The lattice constants show a discontinuity above 6 GPa, which translates into a discontinuity in (e) the  $c/a$  ratio as well as the volume (inset). (f) These discontinuities are also shown in the fractional atomic coordinates within the unit cell.

### III. SUPERTETRAGONAL PHASE UNDER NEGATIVE PRESSURE

#### A. Structure

A fully unconstrained atomic relaxation is performed for all four BaTiO<sub>3</sub> phases where the negative pressure has been artificially introduced into the Cauchy stress tensor for the minimization of the Hellmann-Feynmann forces. This implies that all structural degrees of freedom are optimized, without imposing any crystal structure, which is in stark contrast to a recent first-principle study [38], and more similar to the work of Tinte et al. on PbTiO<sub>3</sub> [39]. It can be found that upon a negative pressure above 6 GPa, the tetragonal phase undergoes an abrupt structural phase transition as observed in the lattice constants and the respective  $c/a$  ratio and volume (see Figure 2d-e). The abrupt increase has been driven by changes in the bond length, quantified by the deviations from the high-symmetric Wyckoff positions (see Figure 2c). Note that this phase transition does not involve any change in the crystal symmetry, and shall therefore be referred to as isosymmetric, which also implies a first-order nature of the phase transition [40].

In addition to the ionic relaxation of the tetragonal phase upon negative pressure, the cubic, orthorhombic

and rhombohedral phases were also structurally optimized for each pressure value (see Supplemental Information). However, none of these phases showed any structural anomaly and therefore were not studied further. Nonetheless, by a comparison of the enthalpy of the different BaTiO<sub>3</sub> phases, it becomes clear that the ST phase will have the lowest enthalpy compared to the others, due to the anomalous volume enhancement. Note that the choice of enthalpy in the energetic comparison is considered appropriate in the study of pressure-induced phase transitions, as also shown earlier [41].

#### B. Dielectric Properties

For each optimized pressure state, the spontaneous polarization ( $P_s$ ) was calculated within the Berry phase theory of polarization [42, 43], as shown in Figure 3a. The anomalous enhancement is again observed for  $P_s$ , moreover, it fully arises from the ionic dipole moment that has been induced by the structural anomaly. To obtain further insight into the dielectric behavior of the ST transition, the optical dielectric tensor ( $\epsilon^\infty$ ) and Born effective charges ( $Z^*$ ) were evaluated.

The transition to a ST phase results in the reduction of the dielectric function, with a manifest discontinuity in the longitudinal component  $\epsilon_{\parallel}^\infty$ . The reduction is more

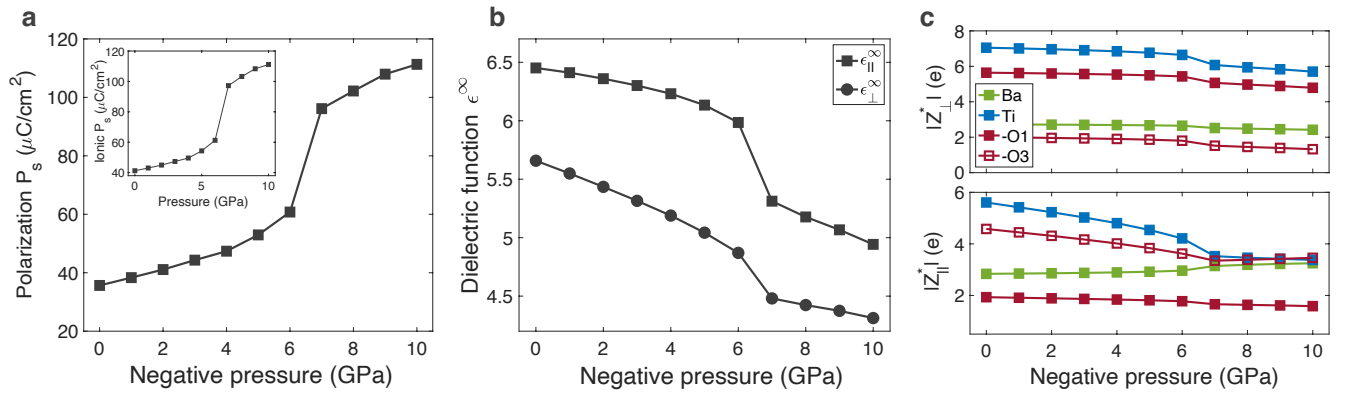


Figure 3. The dielectric component of the supertetragonal phase transition. (a) The polarization as a function of pressure whose abrupt enhancement fully arises from the ionic component (inset). (b) The dielectric function, decomposed into a longitudinal ( $\epsilon_{\parallel}^{\infty}$ ) and transversal in-plane ( $\epsilon_{\perp}^{\infty}$ ) diagonal component. (c) The effective Born charges of each element with its transverse ( $Z_{\perp}^*$ ) and longitudinal ( $Z_{\parallel}^*$ ) diagonal components shown.

pronounced in comparison to the transition to the low-T orthorhombic and rhombohedral phases. Similarly, for the Born charges an abrupt reduction is observed at the transition. More specifically, it can be seen that  $Z_{\parallel}^*$  of titanium drastically reduces from the anomalous value of 5.61 to below its atomic charge of 4. Both trends suggest an enhanced covalency with electrons forming well-defined localized hybrid orbitals with less electron flow and thus a reduced polarizability, as discussed in Sec. II. The negative pressure induced electron localization within strong covalent bonds can also be understood in a simplistic picture where the higher volume dependence of the kinetic energy ( $V^{-2/3}$ ) in comparison to the electrostatic potential energy ( $V^{-1/3}$ ) plays a crucial role in the ST transition that involves a large volume enhancement [44].

### C. Comparison to Biaxial Strain

In addition to the appearance of a ST phase transition upon hydrostatic negative pressure, it was verified whether an in-plane biaxial strain could result in a similar phase transition. To apply a biaxial strain, two different methods were adopted; in both cases, the in-plane lattice component were fixed, while the out-of-plane component is fully relaxed. In the first method (1), the  $(x, y)$  coordinates of the atoms have been fixed, whereas in the second method (2) - considered as the best approximation to the experimental reality - the atoms have been fully relaxed in all three spatial coordinates. The comparison between both biaxial strain methods and the hydrostatic pressure is shown in Figure 4, where for the biaxial strain, the pressure is corresponding to the in-plane stress that has been induced by the applied compressive strain ranging from 0 to  $-7\%$ .

First of all, the induced in-plane stress for the biaxial

method 2 is slightly lower in the transition with a larger  $c$ , which indicates that the atoms attempt to accommodate the in-plane stress by a reordering in which there is an increased out-of-plane distortion.

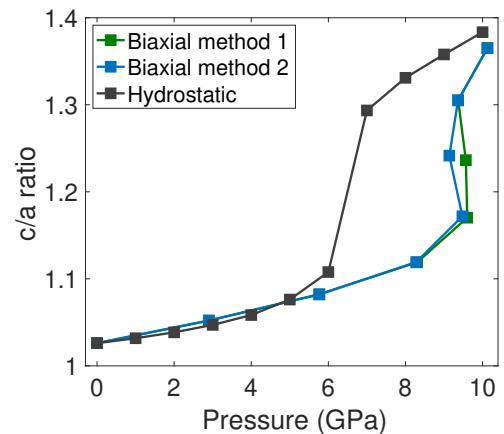


Figure 4. Comparison between hydrostatic and in-plane biaxial strain. The first method (green) corresponds to an ionic relaxation with in-plane atomic coordinates and lattice constants fixed, while the second method optimizes all three spatial coordinates of the atoms, while fixing the in-plane lattice constants.

Secondly, it can be seen that the hydrostatic pressure is much more effective to induce the ST phase as it requires  $\sim 2$  GPa lower pressure values to be applied. However, it should be emphasized that although both ST phases in the hydrostatic and biaxial case have a similar  $c/a$  ratio, they are very distinct in any other aspect. The ST phase induced by a compressive biaxial strain of  $-6\%$  ( $a = b = 3.73 \text{ \AA}$ ) has  $c/a = 1.31$  while for the negative pressure induced ST phase with  $c/a = 1.33$  at 8 GPa has a much larger in-plane lattice constant of  $a = b = 3.89 \text{ \AA}$ . This also means that a smaller change in the  $c$  lattice con-

stant has been induced by biaxial strain, resulting in a lower polarization of  $P_s = 91.1 \mu\text{C}/\text{cm}^2$  for  $c/a = 1.31$  (compared to  $102.2 \mu\text{C}/\text{cm}^2$  with  $c/a = 1.33$  at negative pressure 8 GPa). This confirms that the ST can not be fully established by a biaxial strain, and requires an additional out-of-plane tensile stress. In other words, the ST phase (observed upon negative pressure) is not lying on the Poisson line with  $\sigma_z = 0$  within 6D strain space, although there still exists a first-order structural anomaly along this line. Moreover, it explains why the ST phase can be established for highly biaxial strained  $\text{BiFeO}_3$  where the 6s lone pair provides a stronger internal out-of-plane stress driving it towards a ST structure [21, 22].

#### IV. MICROSCOPIC ORIGIN OF SUPERTETRAGONALITY

The origin of these supertetragonal phases remains poorly understood, with many authors suggesting the breaking of the bond along the tetragonal axis [39, 45, 46], albeit ill-defined what is meant. In case of a true broken bond along the  $c$ -axis of the long Ti–O bond, the coordination number of Ti would reduce to 5, giving rise to a layered structure. Such square pyramidal coordinations has been found in some layered titanium complexes with a short Ti–O bond length of  $1.63 - 1.66 \text{ \AA}$ , which is considered as symptomatic for a double bond [47, 48]. However, this is in contrast to the minimum Ti–O bond length of  $1.77 \text{ \AA}$  found in the ST phase, therefore, the proposal of a true five-fold square pyramidal Ti coordination in the ST phase can be disregarded, and thus the long Ti–O bond along the polar axis can not be considered as fully broken.

Similarly, it could be argued that this change in coordination is indicating a change in the oxidation state of  $\text{Ti}^{4+}$  to  $\text{Ti}^{3+}$ , as in  $\text{LaTiO}_3$ . However, this would mean that Ti has an electron configuration  $3d^1$ , with the electron localized on Ti, similar to ST  $\text{PbVO}_3$  [49]. However, such a valence transition would result in a drastic change in the partial density of states (DOS) of the Ti  $3d$  orbitals, which is not the case. Furthermore, by Bader charge [50] and Mülliken orbital population analysis [51] (see Supplemental Information), no change in the valence state could be inferred. On the other hand, these charge analysis are inconclusive on whether the ST transition can be explained as a drastic change from ionic to covalent bonding, nor does the electron localization function (ELF) shows any significant changes upon the transition (see Supplemental Information).

Hence, the charge density was studied within a plane wave formalism as well as within the projected crystal orbital hamiltonian population (pCOHP) theory to obtain a more detailed picture of the chemical changes that occurs in the isosymmetric phase transition. For the equilibrium tetragonal phase, it can be seen in the DOS (see

Figure 5a) that there is a crystal field splitting of the  $e_g$  and  $t_{2g}$  orbitals that correspondingly form the  $\sigma$ -bond and  $\pi$ -bond, with the bonded orbitals between  $-5 \text{ eV}$  and  $-2 \text{ eV}$ . The valence band maximum (VBM) largely consists of unbonded oxygen  $p$ -orbitals (forming the  $t_{1u}$  and  $t_{2u}$  orbital levels), while the antibonded states of the  $\pi$ -bond ( $t_{2g}^*$ ) form the conduction band minimum (CBM). Upon transitioning, there are several significant changes in the DOS that can be identified.

Firstly, the  $\sigma$ -bonding  $d$ -orbitals remain nearly unchanged throughout the whole pressure range, indicating their minor role in the ST phase transition. On the other hand, the width of the  $(d_{xz}, d_{yz})$  orbital DOS weight decreases, which implies the localization of the electrons within these  $\pi$ -bonded  $d$ -orbitals. Secondly, these latter orbitals are also shifted towards lower energies within the valence band, such that they coincide within the energy range of the  $e_g$  orbital levels. Thirdly, the VBM consisting of non-bonding oxygen  $p$ -orbitals also changes drastically with a vanishing weight of the  $\text{O}_3$  atom, indicating that this atom is fully involved in the bond with titanium upon the ST transition.

However, a complete chemical interpretation of these changes in the electronic DOS remains a delicate task, therefore, the pCOHP was evaluated. This is the DOS weighted by its Hamiltonian matrix element, indicative of the bond strength. These calculations were performed on a  $1 \times 1 \times 2$  supercell in order to properly compare the pCOHP of the short and long Ti–O bond along the polar axis. In this way the bonding (negative pCOHP) and antibonding (positive pCOHP) states that are formed in the tetragonal distortion can be clearly seen in the pCOHP (bottom two rows in Figure 5a). For the short Ti–O bond around the transition, it is again observed that the  $\pi$ -bond weight (both for bonding as antibonding states) has a reduced width, while the bonded states shift to lower energies coinciding with the  $\sigma$ -bonded weight. The first feature indicates that the electron are localized into well-defined hybrid orbital states, which is in agreement with the observations in section III B. The latter feature involves the combination of two effects, namely an enhanced crystal field splitting as well as an increased bond strength (orbital overlap).

The pCOHP of the long Ti–O bond looks very different with nearly equal amount of weight of bonding and antibonding states below the Fermi level, which implies a bond order of zero. Most interestingly, one observes a vanishing of the  $\pi$ -bond pCOHP weight upon the transition to the ST phase at 7 GPa. This implies that there is no orbital overlap of the  $(d_{xz}, d_{yz})$  along the long bond axis, while the  $\sigma$ -bond weight remains. Additionally, no change in the in-plane components of the pCOHP could be inferred (see Supplemental Information). Hence, it can be concluded that the ST first-order phase transition has been mainly driven by a broken  $\pi$ -bond along the long Ti–O bond.

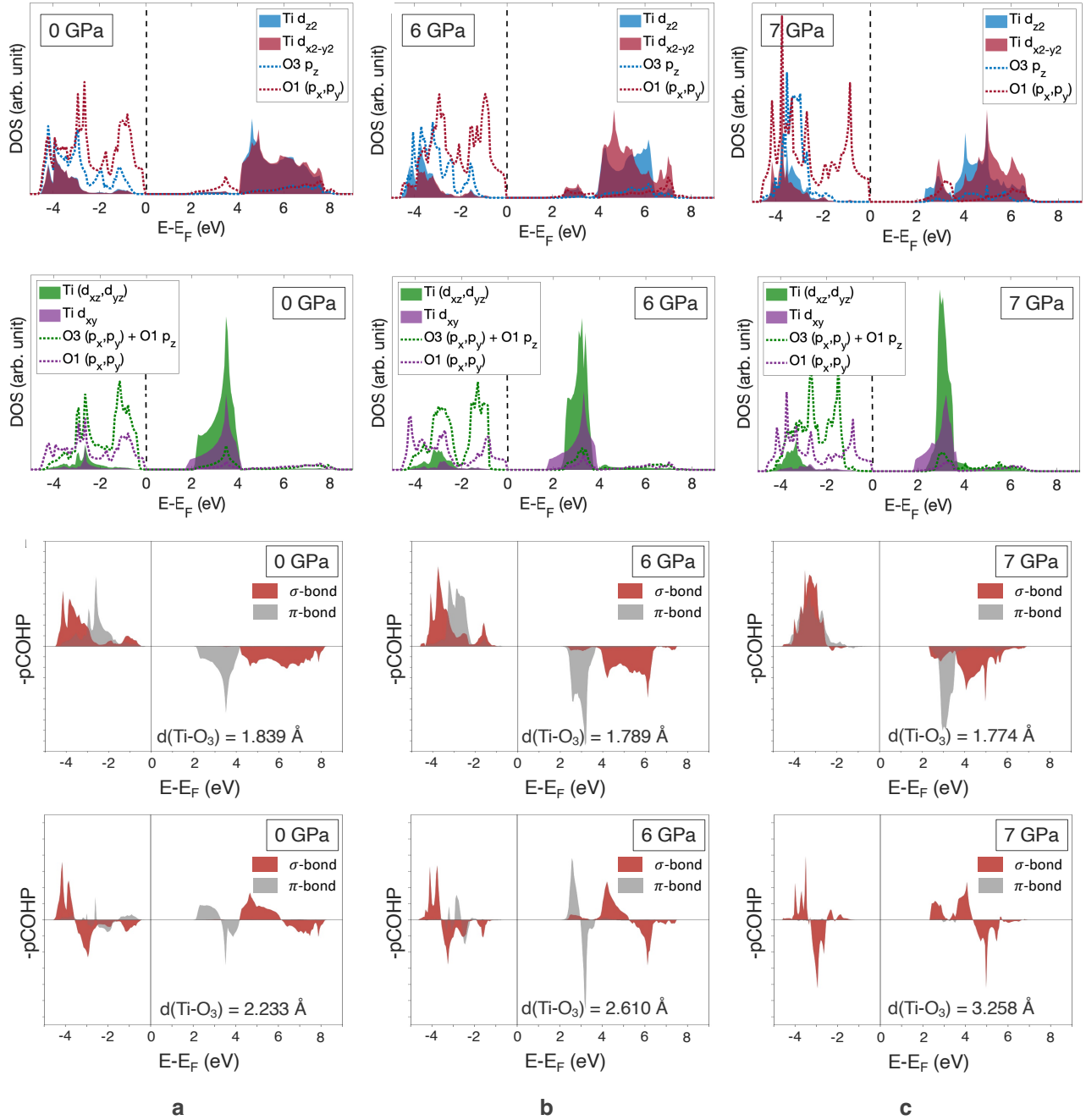


Figure 5. Partial density of states and the projected crystal orbital hamiltonian populations (pCOHP). The partial density of states involved in the  $\sigma$ -bond (top row) and in the  $\pi$ -bond (second row) and the pCOHP evaluated along the short (third row) and long (last row) Ti–O bond of (a) 0 GPa, (b) 6 GPa and (c) 7 GPa. For the pCOHP, the red filling represents the  $\sigma$ -bond contribution (Ti  $d_{z2}$  with O<sub>3</sub>  $p_z$  was taken), and the gray filling represents the  $\pi$ -bond contribution (Ti  $d_{yz}$  with O<sub>3</sub>  $p_y$  was taken).

These observations are confirmed visually by the calculation of the valence charge density (VCD) taken along the (200) plane, as shown in Figure 6. First, a comparison of the VCD of the cubic and tetragonal phase shows the subtle change in the charge density (See Fig. 6a-b), which can mostly easily be seen by an increased density

of the isosurface lines indicating the enhanced covalency upon FE distortion. Upon increasing the negative pressure, the VCD decreases and increases along the long and short Ti–O bond, respectively. In particular, the O<sub>3</sub> anion gains in density perpendicular to the short Ti–O bond, indicating enhancement of the  $\pi$ -bond while the

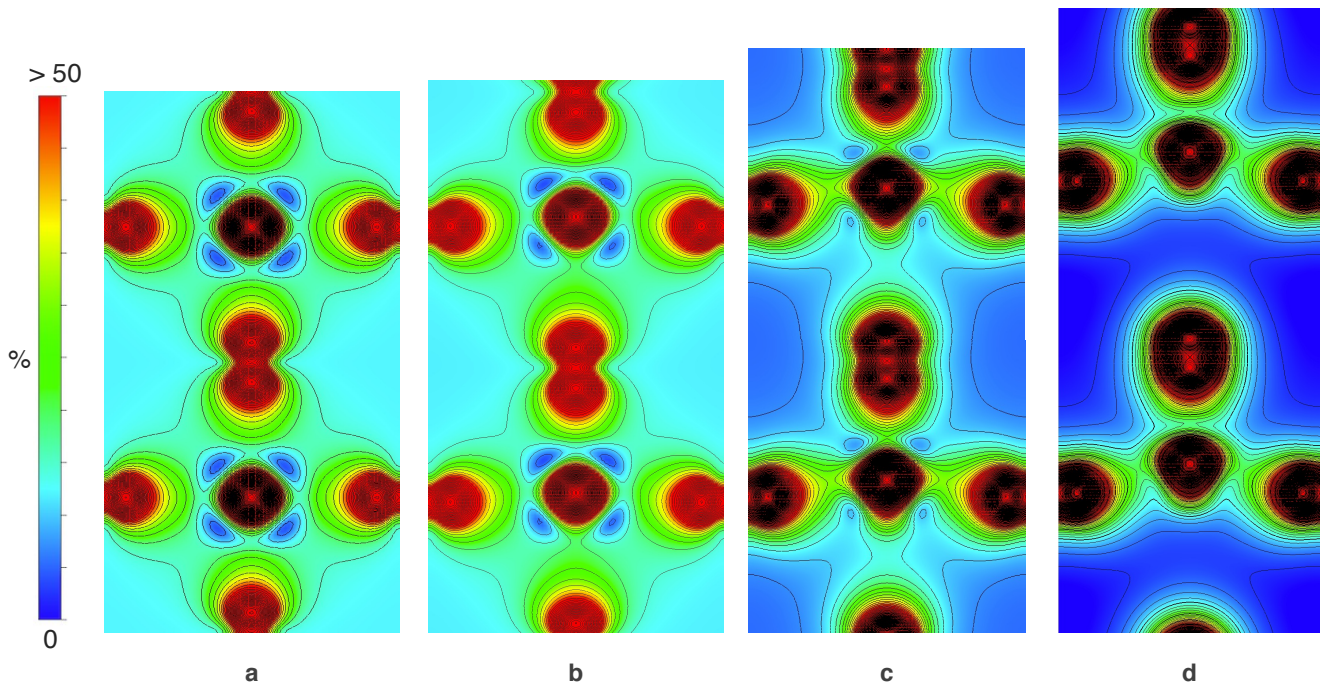


Figure 6. Projected valence band charge density. The valence band charge density taken along the (200) plane in the unit cell of the (a) cubic, (b) tetragonal, (c) tetragonal at 6 GPa, and (d) at 7 GPa.

empty ( $d_{xz}, d_{yz}$ ) lobes of Ti are fully depleted, implying a strong hybridization with the O  $2p$  orbitals.

These findings offers guidance in the understanding of first-order isosymmetric phase transitions [2, 41, 52, 53], which turn out to be often characterized by an anisotropic structural change (ascribed to the high-directionality of the covalent bond). These phase transitions appear in materials where a small anisotropy already exists - often a transition metal off-centring from a high-symmetric position. They form the seed of isosymmetric phase transitions, as they inhibit the covalent bond whose anisotropy can be abruptly enhanced by an external trigger giving rise to a structural first-order transition. Additionally, this sudden enhancement of the existing bond states can also be driven by electron correlations, such as in the case of the Mott metal-insulator transition in  $V_2O_3$  where inducing a change in the orbital overlap of the  $d_{z^2}$  triggers an electronic repulsive force between the neighboring vanadium cations [2].

## V. CONCLUSIONS

Our results proof the existence of a ST phase of  $BaTiO_3$  upon negative pressure of 7 GPa, with an enhanced polarization of  $\sim 95 \mu C/cm^2$ . It was shown that a biaxial strain can not fully induce the ST phase, indicating the opportunities that appear by controlling all three lattice parameters [54]. The microscopic origin of this first-order structural phase transition involves a

charge re-ordering in which the  $\pi$ -bond along the long Ti–O bond completely vanishes while strong  $\pi$ -bonds are formed in a five-fold coordination, preserving the  $Ti^{4+}$  oxidation state. It can be roughly said that the negative pressure opens a new avenue for the electrons to become localized in well-defined covalent bonds along an exceptionally short Ti–O bond, instead of localizing these electrons by additional covalent bonds formed with two ( $Amm2$ ) or three ( $R3m$ ) oxygen atoms. These findings shed light on how isosymmetric phase transitions are driven by subtle changes in their chemical bonding, requiring the need for a local auxiliary atomic orbital description.

## VI. COMPUTATIONAL METHODS

All density functional theory (DFT) calculations were performed by the Vienna *ab initio* simulation package (VASP) [55]. The interactions between electrons and ions were described by the projector augmented wave (PAW) potentials [56], with the electronic wave functions expanded with a large cutoff energy of 900 eV. The PBEsol exchange-correlation functional [57] was used for all calculations. For the structural relaxation, a force convergence criterion of  $0.005 \text{ eV}/\text{\AA}$  was used with the Brillouin zone (BZ) sampled by a  $12 \times 12 \times 12$   $\Gamma$ -centered  $k$ -scheme. Phonon dispersions and dielectric properties were calculated self-consistently on the basis of density functional perturbation theory (DFPT) and with the

use of the PHONOPY package [58]. For the electronic and dielectric properties a denser  $24 \times 24 \times 24$  mesh was used with energy convergence criterion of  $10^{-6}$  eV. The Berry phase method as implemented in VASP was adopted for the calculation of the polarization [42, 43]. For the crystal orbital hamiltonian population (pCOHP), the LOBSTER package [59, 60] was used with basis sets Ba ( $5s, 5p, 5d, 6s$ ), Ti ( $3s, 3p, 3d, 4s$ ) and O ( $2s, 2p$ ) with a minimal charge spilling.

### ACKNOWLEDGEMENTS

Part of this work was financially supported by the KU Leuven Research Funds, Project No. C14/21/083, iBOF/21/084, No. KAC24/18/056 and No. C14/17/080 as well as the Research Funds of the INTERREG-E-TEST Project (EMR113) and INTERREG-VL-NL-ETPATHFINDER Project (0559). Part of the compu-

tational resources and services used in this work were provided by the VSC (Flemish Supercomputer Center) funded by the Research Foundation Flanders (FWO) and the Flemish government.

### AUTHOR CONTRIBUTIONS

These results were obtained within the framework of the doctoral training of S.M. supervised by J.-P.L., M.H. and J.W.S. S.M. performed all calculations and wrote the manuscript with contributions and comments from all authors.

### COMPETING INTERESTS

The authors declare no competing interests.

## Supplemental Material

### A. Structure of BaTiO<sub>3</sub> Phases Under Negative Pressure

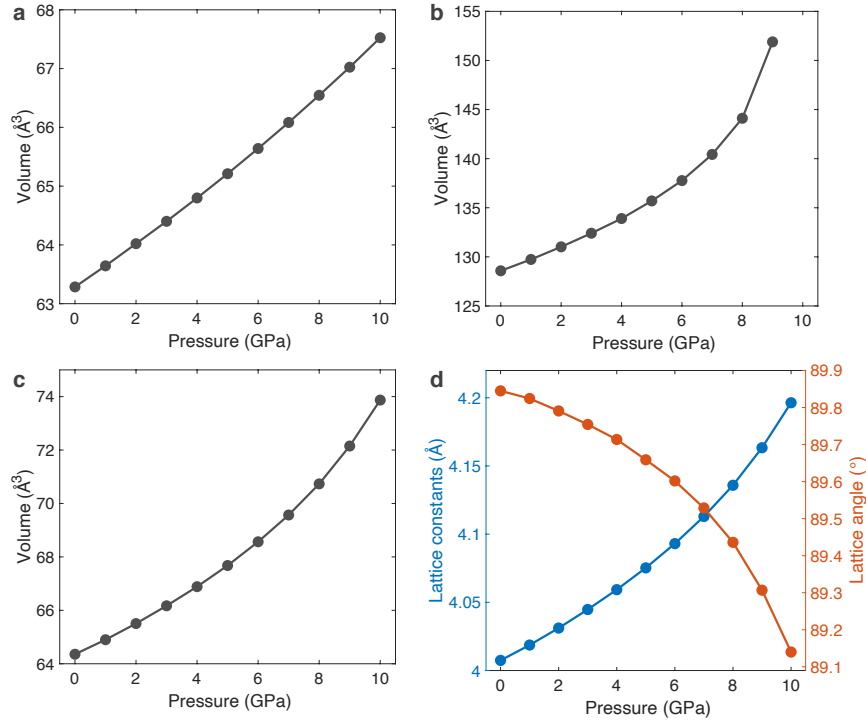


Figure 7. Structure of BaTiO<sub>3</sub> phases under negative pressure. The volume under negative pressure of the (a) cubic (b) orthorhombic and (c) rhombohedral under negative pressure. (d) The structural parameters of the rhombohedral phase.



## B. Enthalpy Comparison

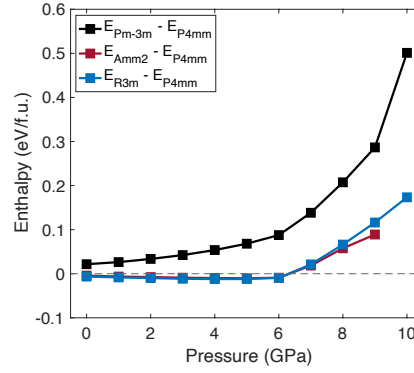


Figure 8. Enthalpy comparison of the cubic ( $Pm\bar{3}m$ ), tetragonal ( $P4mm$ ), orthorhombic ( $Amm2$ ) and rhombohedral ( $R3m$ ).

## C. Atomic charge analysis

	0 GPa	6 GPa	7 GPa	0 GPa	6 GPa	7 GPa
Ba	1.568	1.569	1.574	2.11	1.96	1.83
Ti	2.129	2.109	2.119	0.82	1.00	1.19
O <sub>1</sub>	-1.240	-1.249	-1.256	-0.99	-0.80	-1.03
O <sub>3</sub>	-1.218	-1.180	-1.187	-0.95	-0.93	-0.95

Table III. The Bader atomic charges (left) and Mülliken charges (right).

## D. Electron localization function

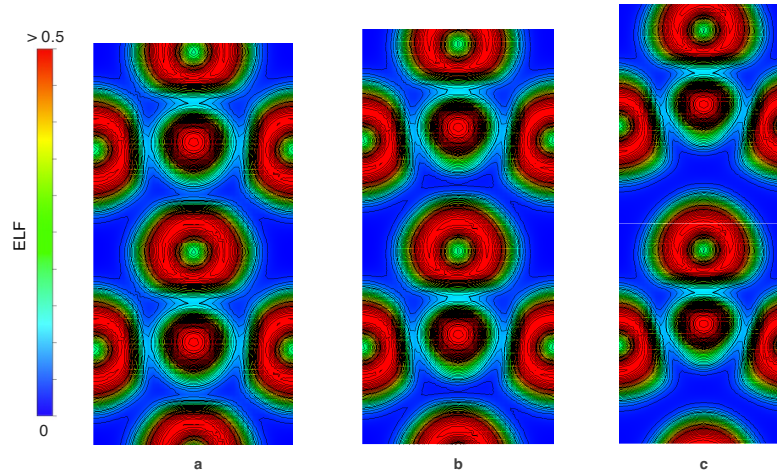


Figure 9. Electron localization function as a function of pressure. ELF taken along the (200) plane for (a) 0 GPa, (b) 6 GPa and (c) 7 GPa.

### E. In-plane pCOHP

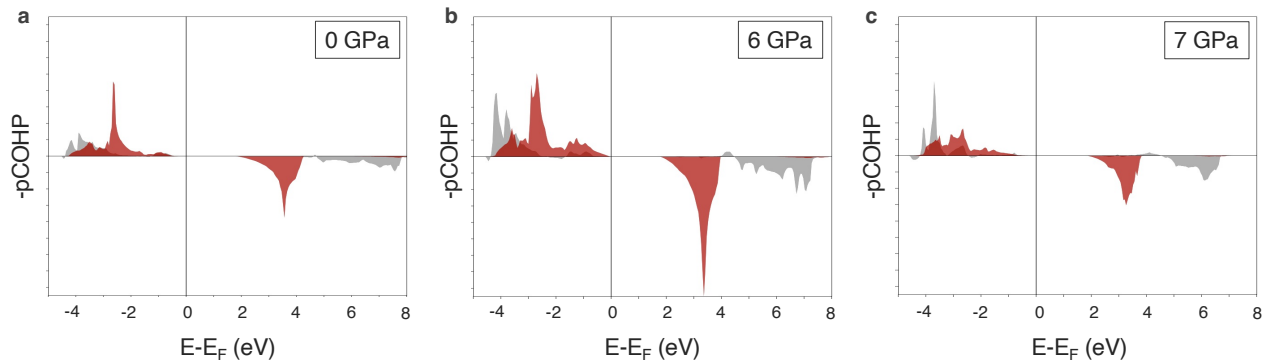


Figure 10. The projected crystal orbital hamiltonian population (pCOHP) of the in-plane bonds. Red and grey shaded area representing the  $\sigma$ -bond (Ti  $d_{x^2-y^2}$  with  $O_1 p_x$  was taken) and the  $\pi$ -bond (Ti  $d_{xy}$  with  $O_1 p_y$  was taken), respectively.

- 
- [1] J. P. Locquet, J. Perret, J. Fompeyrine, E. Mächler, J. W. Seo, and G. Van Tendeloo. Doubling the critical temperature of  $\text{La}_{1.9}\text{Sr}_{0.1}\text{CuO}_4$  using epitaxial strain. *Nature*, 394(6692):453–456, 1998.
  - [2] P. Homm, M. Menghini, J. W. Seo, S. Peters, and J. P. Locquet. Room temperature mott metal–insulator transition in  $\text{v}_2\text{o}_3$  compounds induced via strain-engineering. *APL Materials*, 9(2):021116, 2021.
  - [3] Tanusri Saha-Dasgupta. Double perovskites with 3d and 4d/5d transition metals: compounds with promises. 7(1):014003, jan 2020.
  - [4] Guo-Hong Cai, Martha Greenblatt, and Man-Rong Li. Polar magnets in double corundum oxides. *Chemistry of Materials*, 29(13):5447–5457, 07 2017.
  - [5] Nicole A. Benedek, Andrew T. Mulder, and Craig J. Fennie. Polar octahedral rotations: A path to new multifunctional materials. *Journal of Solid State Chemistry*, 195:11–20, 2012. Polar Inorganic Materials: Design Strategies and Functional Properties.
  - [6] James M. Rondinelli and Craig J. Fennie. Octahedral rotation-induced ferroelectricity in cation ordered perovskites. *Advanced Materials*, 24(15):1961–1968, 2012.
  - [7] H. Zheng, J. Wang, S. E. Lofland, Z. Ma, L. Mohaddes-Ardabili, T. Zhao, L. Salamanca-Riba, S. R. Shinde, S. B. Ogale, F. Bai, D. Viehland, Y. Jia, D. G. Schlom, M. Wuttig, A. Roytburd, and R. Ramesh. Multiferroic  $\text{batio}_3\text{-cofe}_2\text{o}_4$  nanostructures. *Science*, 303(5658):661–663, 2004.
  - [8] Judith MacManus-Driscoll, Ady Suwardi, Ahmed Kursumovic, Zhenxing Bi, Chen-Fong Tsai, Haiyan Wang, Quanxi Jia, and Oon Jew Lee. New strain states and radical property tuning of metal oxides using a nanocomposite thin film approach. *APL Materials*, 3(6):062507, 2015.
  - [9] Eun-Mi Choi, Angelo Di Bernardo, Bonan Zhu, Ping Lu, Hen Alpern, Kelvin H. L. Zhang, Tamar Shapira, John Feighan, Xing Sun, Jason Robinson, Yossi Paltiel, Oded Millo, Haiyan Wang, Quanxi Jia, and Judith L. MacManus-Driscoll. 3d strain-induced superconductivity in  $\text{La}_2\text{CuO}_4+\delta$  using a simple vertically aligned nanocomposite approach. *Science Advances*, 5(4), 2019.
  - [10] Yisong Lin, Eun-Mi Choi, Ping Lu, Xing Sun, Rui Wu, Chao Yun, Bonan Zhu, Haiyan Wang, Weiwei Li, Tuhin Maity, and Judith MacManus-Driscoll. Vertical strain-driven antiferromagnetic to ferromagnetic phase transition in  $\text{eutio}_3$  nanocomposite thin films. *ACS Applied Materials & Interfaces*, 12(7):8513–8521, 02 2020.
  - [11] Xiyuan Zhang, Ruixing Xu, Xingyao Gao, Yanda Ji, Fengjiao Qian, Jiyu Fan, Haiyan Wang, Weiwei Li, and Hao Yang. Negative-pressure enhanced ferroelectricity and piezoelectricity in lead-free  $\text{batio}_3$  ferroelectric nanocomposite films. *J. Mater. Chem. C*, 8:8091–8097, 2020.
  - [12] Oon Jew Lee, Shikhar Misra, Haiyan Wang, and J. L. MacManus-Driscoll. Ferroelectric/multiferroic self-assembled vertically aligned nanocomposites: Current and future status. *APL Materials*, 9(3):030904, 2021.
  - [13] R. A. McKee, F. J. Walker, and M. F. Chisholm. Crystalline oxides on silicon: The first five monolayers. *Phys. Rev. Lett.*, 81:3014–3017, Oct 1998.
  - [14] G. J. Norga, C. Marchiori, C. Rossel, A. Guiller, J. P. Locquet, H. Siegwart, D. Caimi, J. Fompeyrine, J. W. Seo, and Ch. Dieker. Solid phase epitaxy of  $\text{srTiO}_3$  on  $(\text{Ba},\text{Sr})\text{O}/\text{Si}(100)$ : The relationship between oxygen stoichiometry and interface stability. *Journal of Applied Physics*, 99(8):084102, 2006.
  - [15] Chiara Marchiori, M. Sousa, A. Guiller, H. Siegwart, J.-P. Locquet, J. Fompeyrine, G. J. Norga, and J. W. Seo. Thermal stability of the  $\text{srTiO}_3/(\text{Ba},\text{Sr})\text{O}$  stacks epitaxially grown on Si. *Applied Physics Letters*, 88(7):072913, 2006.

- [16] Stefan Abel, Thilo Stöferle, Chiara Marchiori, Christophe Rossel, Marta D. Rossell, Rolf Erni, Daniele Caimi, Marilyne Sousa, Alexei Chelnokov, Bert J. Offrein, and Jean Fompeyrine. A strong electro-optically active lead-free ferroelectric integrated on silicon. *Nature Communications*, 4(1):1671, 2013.
- [17] Stefan Abel, Felix Eltes, J. Elliott Ortmann, Andreas Messner, Pau Castera, Tino Wagner, Darius Urbonas, Alvaro Rosa, Ana M. Gutierrez, Domenico Tulli, Ping Ma, Benedikt Baeuerle, Arne Josten, Wolfgang Heni, Daniele Caimi, Lukas Czornomaz, Alexander A. Demkov, Juerg Leuthold, Pablo Sanchis, and Jean Fompeyrine. Large poekels effect in micro- and nanostructured barium titanate integrated on silicon. *Nature Materials*, 18(1):42–47, 2019.
- [18] Binbin Chen, Nicolas Gauquelin, Nives Strkalj, Sizhao Huang, Ufuk Halisdemir, Minh Duc Nguyen, Daen Jannis, Martin F. Sarott, Felix Eltes, Stefan Abel, Matjaž Spreitzer, Manfred Fiebig, Morgan Trassin, Jean Fompeyrine, Johan Verbeeck, Mark Huijben, Guus Rijnders, and Gertjan Koster. Signatures of enhanced out-of-plane polarization in asymmetric batio3 superlattices integrated on silicon. *Nature Communications*, 13(1):265, 2022.
- [19] Jin Wang, Ben Wylie-van Eerd, Tomas Sluka, Cosmin Sandu, Marco Cantoni, Xian-Kui Wei, Alexander Kvasov, Leo John McGilly, Pascale Gemeiner, Brahim Dkhil, Alexander Tagantsev, Joe Trodahl, and Nava Setter. Negative-pressure-induced enhancement in a freestanding ferroelectric. *Nature Materials*, 14(10):985–990, 2015.
- [20] Jing Sun, Qiang Li, He Zhu, Zhanning Liu, Kun Lin, Na Wang, Qinghua Zhang, Lin Gu, Jinxia Deng, Jun Chen, and Xianran Xing. Negative-pressure-induced large polarization in nanosized pbtio3. *Advanced Materials*, 32(48):2002968, 2020.
- [21] H. Béa, B. Dupé, S. Fusil, R. Mattana, E. Jacquet, B. Warot-Fonrose, F. Wilhelm, A. Rogalev, S. Petit, V. Cros, A. Anane, F. Petroff, K. Bouzouane, G. Geneste, B. Dkhil, S. Lisenkov, I. Ponomareva, L. Bellaiche, M. Bibes, and A. Barthélémy. Evidence for room-temperature multiferroicity in a compound with a giant axial ratio. *Phys. Rev. Lett.*, 102:217603, May 2009.
- [22] J. X. Zhang, Q. He, M. Trassin, W. Luo, D. Yi, M. D. Rossell, P. Yu, L. You, C. H. Wang, C. Y. Kuo, J. T. Heron, Z. Hu, R. J. Zeches, H. J. Lin, A. Tanaka, C. T. Chen, L. H. Tjeng, Y.-H. Chu, and R. Ramesh. Microscopic origin of the giant ferroelectric polarization in tetragonal-like bifeo<sub>3</sub>. *Phys. Rev. Lett.*, 107:147602, Sep 2011.
- [23] Simuck F. Yuk, Krishna Chaitanya Pitike, Serge M. Nakhmanson, Markus Eisenbach, Ying Wai Li, and Valentino R. Cooper. Towards an accurate description of perovskite ferroelectrics: exchange and correlation effects. *Scientific Reports*, 7(1):43482, 2017.
- [24] Ulrich Aschauer and Nicola A Spaldin. Competition and cooperation between antiferrodistortive and ferroelectric instabilities in the model perovskite SrTiO<sub>3</sub>. *Journal of Physics: Condensed Matter*, 26(12):122203, mar 2014.
- [25] James W. Edwards, Rudolph Speiser, and Herrick L. Johnston. Structure of barium titanate at elevated temperatures. *Journal of the American Chemical Society*, 73(6):2934–2935, 06 1951.
- [26] Gerald Burns and F.H. Dacol. Polarization in the cubic phase of batio3. *Solid State Communications*, 42(1):9–12, 1982.
- [27] J. Harada, T. Pedersen, and Z. Barnea. X-ray and neutron diffraction study of tetragonal barium titanate. *Acta Crystallographica Section A*, 26(3):336–344, May 1970.
- [28] Michael S. Shumate. Interferometric measurement of large indices of refraction. *Appl. Opt.*, 5(2):327–331, Feb 1966.
- [29] H. H. Wieder. Electrical behavior of barium titanate single crystals at low temperatures. *Phys. Rev.*, 99:1161–1165, Aug 1955.
- [30] G. H. Kwei, A. C. Lawson, S. J. L. Billinge, and S. W. Cheong. Structures of the ferroelectric phases of barium titanate. *The Journal of Physical Chemistry*, 97(10):2368–2377, 03 1993.
- [31] Don Berlincourt and Hans Jaffe. Elastic and piezoelectric coefficients of single-crystal barium titanate. *Phys. Rev.*, 111:143–148, Jul 1958.
- [32] M. Atanasov and D. Reinen. Density functional studies on the lone pair effect of the trivalent group (v) elements: I. electronic structure, vibronic coupling, and chemical criteria for the occurrence of lone pair distortions in ax<sub>3</sub> molecules (a=n to bi; x=h, and f to i). *The Journal of Physical Chemistry A*, 105(22):5450–5467, 06 2001.
- [33] H. Thomann. A covalency model of ferroic phase transitions in perovskites. *Ferroelectrics*, 73(1):183–199, 1987.
- [34] Ronald E. Cohen. Origin of ferroelectricity in perovskite oxides. *Nature*, 358(6382):136–138, 1992.
- [35] Katarzyna Tkacz-Śmiech, A. Koleżyński, and W. S. Ptak. Chemical bond in ferroelectric perovskites. *Ferroelectrics*, 237(1):57–64, 2000.
- [36] Katarzyna Tkacz-Śmiech, Andrzej Koleżyński, and W.S. Ptak. Crystal-chemical aspects of phase transitions in barium titanate. *Solid State Communications*, 127(8):557–562, 2003.
- [37] Andrzej Koleżyński and Katarzyna Tkacz-Śmiech. From the molecular picture to the band structure of cubic and tetragonal barium titanate. *Ferroelectrics*, 314(1):123–134, 2005.
- [38] Namrata Jaykhedkar, Nilakantha Tripathy, Vaishali Shah, Bhalchandra Pujari, and S. Premkumar. A comprehensive study of pressure dependent phase transitions in ferroelectric pbtio<sub>3</sub>, pbzro<sub>3</sub> and batio<sub>3</sub>. *Materials Chemistry and Physics*, 254:123545, 2020.
- [39] Silvia Tinte, Karin M. Rabe, and David Vanderbilt. Anomalous enhancement of tetragonality in pbtio<sub>3</sub> induced by negative pressure. *Phys. Rev. B*, 68:144105, Oct 2003.
- [40] A. G. Christy. Isosymmetric structural phase transitions: phenomenology and examples. *Acta Crystallographica Section B*, 51(5):753–757, Oct 1995.
- [41] J. W. Allen and Richard M. Martin. Kondo volume collapse and the  $\gamma \rightarrow \alpha$  transition in cerium. *Phys. Rev. Lett.*, 49:1106–1110, Oct 1982.
- [42] R. W. Nunes and Xavier Gonze. Berry-phase treatment of the homogeneous electric field perturbation in insulators. *Phys. Rev. B*, 63:155107, Mar 2001.
- [43] Ivo Souza, Jorge Íñiguez, and David Vanderbilt. First-principles approach to insulators in finite electric fields. *Phys. Rev.*

*Lett.*, 89:117602, Aug 2002.

- [44] Choong-Shik Yoo. Chemistry under extreme conditions: Pressure evolution of chemical bonding and structure in dense solids. *Matter and Radiation at Extremes*, 5(1):018202, 2020.
- [45] Alison J. Hatt, Nicola A. Spaldin, and Claude Ederer. Strain-induced isosymmetric phase transition in bifeo<sub>3</sub>. *Phys. Rev. B*, 81:054109, Feb 2010.
- [46] Netanela Cohen and Oswaldo Diéguez. Supertetragonal phases of perovskite oxides: Insights from electronic structure calculations. *Israel Journal of Chemistry*, 60(8-9):833–841, 2020.
- [47] M. A. Roberts, G. Sankar, J. M. Thomas, R. H. Jones, H. Du, J. Chen, W. Pang, and R. Xu. Synthesis and structure of a layered titanosilicate catalyst with five-coordinate titanium. *Nature*, 381(6581):401–404, 1996.
- [48] Maria Batuk, Dmitry Batuk, Artem M. Abakumov, and Joke Hadermann. Pb<sub>5</sub>Fe<sub>3</sub>TiO<sub>11</sub>Cl: A rare example of ti(IV) in a square pyramidal oxygen coordination. *Journal of Solid State Chemistry*, 215:245–252, 2014.
- [49] John B Goodenough and Jianshi Zhou. Varied roles of pb in transition-metal pbmo<sub>3</sub> perovskites (m = ti, v, cr, mn, fe, ni, ru). *Science and Technology of Advanced Materials*, 16(3):036003, 2015. PMID: 27877814.
- [50] Richard F. W. Bader. A quantum theory of molecular structure and its applications. *Chemical Reviews*, 91(5):893–928, 07 1991.
- [51] R. S. Mulliken. Electronic population analysis on lcao–mo molecular wave functions. i. *The Journal of Chemical Physics*, 23(10):1833–1840, 1955.
- [52] L. Ehm, K. Knorr, L. Peters, S. Rath, and W. Depmeier. Pressure induced phase transition in fe<sub>0.47</sub>nbs<sub>2</sub> studied by powder x-ray diffraction. *Journal of Alloys and Compounds*, 429(1):82–86, 2007.
- [53] J. Haines, J. M. Léger, and O. Schulte. High-pressure isosymmetric phase transition in orthorhombic lead fluoride. *Phys. Rev. B*, 57:7551–7555, Apr 1998.
- [54] Simon Mellaerts, Valeri Afanas’ev, Jin Won Seo, Michel Houssa, and Jean-Pierre Locquet. Efficient direct band-gap transition in germanium by three-dimensional strain. *ACS Applied Materials & Interfaces*, 13(26):30941–30949, 07 2021.
- [55] G. Kresse and J. Furthmüller. Efficient iterative schemes for ab initio total-energy calculations using a plane-wave basis set. *Phys. Rev. B*, 54:11169–11186, Oct 1996.
- [56] G. Kresse and D. Joubert. From ultrasoft pseudopotentials to the projector augmented-wave method. *Phys. Rev. B*, 59:1758–1775, Jan 1999.
- [57] Gábor I. Csonka, John P. Perdew, Adrienn Ruzsinszky, Pier H. T. Philipsen, Sébastien Lebègue, Joachim Paier, Oleg A. Vydrov, and János G. Ángyán. Assessing the performance of recent density functionals for bulk solids. *Phys. Rev. B*, 79:155107, Apr 2009.
- [58] A. Togo and I. Tanaka. First principles phonon calculations in materials science. *Scr. Mater.*, 108:1–5, Nov 2015.
- [59] Richard Dronskowski and Peter E. Blochl. Crystal orbital hamilton populations (cohp): energy-resolved visualization of chemical bonding in solids based on density-functional calculations. *The Journal of Physical Chemistry*, 97(33):8617–8624, 08 1993.
- [60] Ryky Nelson, Christina Ertural, Janine George, Volker L. Deringer, Geoffroy Hautier, and Richard Dronskowski. Lobster: Local orbital projections, atomic charges, and chemical-bonding analysis from projector-augmented-wave-based density-functional theory. *Journal of Computational Chemistry*, 41(21):1931–1940, 2020.